

## Probing angle-dependent thermal conductivity in twisted bilayer MoSe<sub>2</sub>

Manab Mandal <sup>1,2</sup>, Nikhilesh Maity<sup>3</sup>, Prahalad Kanti Barman<sup>2,4</sup>, Ashutosh Srivastava <sup>3</sup>, Abhishek K. Singh,<sup>3</sup>  
Pramoda K. Nayak <sup>2,4,5,\*</sup> and Kanikrishnan Sethupathi <sup>1,2,†</sup>

<sup>1</sup>Low temperature physics lab, Department of Physics, Indian Institute of Technology Madras, Chennai 600 036, India

<sup>2</sup>Department of Physics, Indian Institute of Technology Madras, Chennai 600 036, India

<sup>3</sup>Materials Research Centre, Indian Institute of Science, Bangalore-560012, India

<sup>4</sup>2D Materials Research and Innovation Group, Indian Institute of Technology Madras, Chennai-600036, India

<sup>5</sup>Centre for Nano and Material Sciences, Jain (Deemed-to-be University), Jain Global Campus, Kanakapura, Bangalore 562112, India



(Received 26 June 2023; revised 6 September 2023; accepted 8 September 2023; published 29 September 2023)

Twisted bilayer (t-BL) transition-metal dichalcogenides (TMDCs) have attracted considerable attention in recent years due to their distinctive electronic properties, which arise due to the moiré superlattices that lead to the emergence of flat bands and correlated electron phenomena. Also, these materials can exhibit interesting thermal properties, including a reduction in thermal conductivity. In this paper, we report the thermal conductivity of monolayer (1L) and t-BL MoSe<sub>2</sub> at some specific twist angles around two symmetric stacking *AB* (0°) and *AB'* (60°) and one intermediate angle (31°) using the optothermal Raman technique. The observed thermal conductivity values are found to be  $13 \pm 1$ ,  $23 \pm 3$ , and  $30 \pm 4$  Wm<sup>-1</sup> K<sup>-1</sup> for twist angle  $[\theta] = 58^\circ, 31^\circ$ , and  $3^\circ$ , respectively, which are well supported by our first-principles calculation results. The reduction in thermal conductivity in t-BL MoSe<sub>2</sub> compared to monolayer ( $38 \pm 4$  Wm<sup>-1</sup> K<sup>-1</sup>) can be explained by the occurrence of phonon scattering caused by the formation of a moiré superlattice. Herein, the emergence of multiple folded phonon branches and modification in the Brillouin zone caused by in-plane rotation are also accountable for the decrease in thermal conductivity observed in t-BL MoSe<sub>2</sub>. The theoretical phonon lifetime study and electron localization function analysis further reveals the origin of angle-dependent thermal conductivity in t-BL MoSe<sub>2</sub>. This work paves the way towards tuning the angle-dependent thermal conductivity for any bilayer TMDCs system.

DOI: [10.1103/PhysRevB.108.115439](https://doi.org/10.1103/PhysRevB.108.115439)

### I. INTRODUCTION

Fourier's law of heat conduction is based on the assumption of a continuous temperature field, which is valid only for macroscopic systems where the number of particles is very large. At the microscopic scale (individual atoms or molecules), the concept of temperature becomes more complex, and the continuous temperature field assumption breaks down because of the dimensional limitation [1], thermal rectification [2], and ballistic transport [3]. Hence, the study of thermal conductivity in two-dimensional (2D) limits is significant for both fundamental science [1–3] as well as in technological applications [4–6]. On the other hand, 2D materials, including graphene and transition-metal dichalcogenides (TMDCs), are frequently used in optoelectronic [4], biological monitoring [5], and energy storage [6] devices because of their outstanding optical, electrical, and mechanical characteristics. These materials also possess unique thermal properties that exhibit notable distinction compared to their bulk counterparts due to the reduced dimensionality and the confinement of phonons [7]. In order to enhance heat dissipation in optoelectronic devices, it is essential to

study the thermal conductivities of these materials. Recently Balandin *et al.* reported lower thermal conductivity in monolayer TMDCs compared to a few-layer one, which corresponds to the inverse trend seen in the widely researched 2D materials, for example, in graphene [8]. Therefore, in order to understand this ambiguity in thermal conductivity values of 2D materials with reference to layer number, more rigorous experiments and theoretical models are required. Particularly in their few-layer versions [9–23], TMDCs are extremely fascinating for use in electrical, optical, and thermal applications. Despite extensive research on electron transport in well-explored TMDCs materials like MoS<sub>2</sub>, WS<sub>2</sub>, WSe<sub>2</sub>, and MoSe<sub>2</sub>, the number of experimental reports [24] published on thermal transport is very limited. In addition, MoSe<sub>2</sub> exhibits low thermal conductivity compared to other TMDC materials, which makes it an excellent thermoelectric material [25]. Compared to monolayer MoS<sub>2</sub> and WS<sub>2</sub>, thermal conductivities of monolayer MoSe<sub>2</sub> predicted from atomistic simulations show inconsistent values, varying from 17.6 [25] to 54 Wm<sup>-1</sup> K<sup>-1</sup> [26]. Most of the investigations reported so far concentrate on either monolayer, bilayer or bulk MoSe<sub>2</sub>. However, a systematic variation in thermal conductivity with reference to twist angle is missing in the literature. Moreover, the thermal conductivity of a system with a twisted bilayer (t-BL) is affected by the rotation of the atomic planes to the increased number of phonon scattering sites, which is

\*pramoda.nayak@jainuniversity.ac.in

†ksethu@iitm.ac.in

due to the incorporation of moiré superlattice. The change in the phonon dispersion due to moiré superlattices leads to the emergence of phonon minibands, which can be used to enhance phonon transport in specific directions. In this study, we report the thermal conductivities of atmospheric pressure chemical vapor deposition (APCVD)-grown monolayer (1L) MoSe<sub>2</sub> as well as t-BL MoSe<sub>2</sub> using the optothermal Raman technique [8–27] for selected twist angles. The observed thermal conductivity values were found to be  $13 \pm 1$ ,  $23 \pm 3$  and  $30 \pm 4 \text{ W m}^{-1} \text{ K}^{-1}$  for twist angle  $[\theta] = 58^\circ, 31^\circ$ , and  $3^\circ$ , respectively. In the case of 1L, the thermal conductivity was revealed to be  $38 \pm 4 \text{ W m}^{-1} \text{ K}^{-1}$ , which was larger than the bilayer. Such variation in thermal conductivity was approximated using first-principles calculations, which supports our experimental findings. This study paves the way to explore the twist angle-dependent thermal conductivity for other bilayer TMDCs as well as heterostructures.

## II. MATERIAL AND METHODS

APCVD was used to grow 1L MoSe<sub>2</sub> flakes, as reported in our earlier study [28]. In a typical run, a ceramic boat containing MoO<sub>3</sub> (60 mg) precursors was positioned in a heating-zone center of a quartz-tube furnace of 2 inches in diameter. In the same quartz tube, a quartz boat was positioned at upstream (in the low-temperature zone) and filled with 100 mg of Se powder. Two pieces of sapphire substrates were positioned at downstream with a gap of 2 mm and were placed on the ceramic boat containing MoO<sub>3</sub> powder. A typical temperature of 700 °C and 285 °C was used to heat the MoO<sub>3</sub> and Se precursors, respectively, with an increased rate of 25 °C per minute. The growth period was set for 45 min, and the Ar:H<sub>2</sub> was kept at 60:12 sccm during the growth process. Finally, in the presence of an Ar atmosphere, the furnace had been brought down to ambient temperature.

The technique of aided transfer using poly(methyl methacrylate) (PMMA) was employed to transfer the 1L MoSe<sub>2</sub> flakes over SiO<sub>2</sub> (300 nm)/Si substrate ( $1 \times 1 \text{ cm}^2$ ), which were grown in their natural state on sapphire. The MoSe<sub>2</sub>/sapphire substrate was subsequently spin coated for 60 s at 4000 rpm, after which a few drops of PMMA (677 °C) were applied until the entire surface was covered. The sample was spin coated and then put on a heated plate for roughly 30 min at 120 °C, and around all four edges of the substrate with PMMA coating were scraped with a sharp blade up to 1 mm inside to provide an easy-to-clean border and simple passage for gripping the substrate from all the sides. In order to facilitate the separation of PMMA from the sapphire substrate, a tiny amount of deionized (DI) water was applied to the PMMA/sapphire interface. The hydrophobic characteristic of MoSe<sub>2</sub> prevents the water drop from covering the surface; instead, it assists in hydrating at the interface of sapphire and PMMA-coated MoSe<sub>2</sub> flakes. Using a pointed tweezer, PMMA-coated MoSe<sub>2</sub> film was pilled from the sapphire substrate. For better cleanliness, it was rinsed twice with DI water for 2 min each time. Then, the floating PMMA/MoSe<sub>2</sub> was put onto the SiO<sub>2</sub>/Si substrate. The PMMA coating was subsequently put away by submerging the sample in warm acetone for an entire hour. Here, the required MoSe<sub>2</sub> on SiO<sub>2</sub> (300 nm)/Si was eventually achieved. In order to get t-BL

MoSe<sub>2</sub>, the above process was repeated with the use of as-prepared MoSe<sub>2</sub>/(SiO<sub>2</sub>/Si) as substrate instead of (SiO<sub>2</sub>/Si) followed by cleaning of the PMMA layer using warm acetone. In this process, bilayer MoSe<sub>2</sub> flakes with different stacking orientations were fabricated.

Optical microscopy (OM) images were captured using a Nikon (ECLIPSE LV100ND) microscope with a 100× objective lens and a numerical aperture (NA) of 0.95. Room-temperature low-frequency Raman (LFR) measurements were performed using a “confocal Raman spectrometer” (Renishaw, in Via Reflex). The spectrometer had a backscattering geometry under the same 532-nm laser excitation. Using an ultralow-frequency filter and a 100× objective with a NA of around 0.8, LFR spectra were taken using a confocal Raman spectrometer (LabRam 800, Horiba Jobin Yvon) having “backscattering geometry.” The measurements were carried out with a  $50 \times$  (NA  $\sim 0.55$ ) with a long working distance along with a 633-nm laser excitation. The laser spot diameter of around 1.4 μm was employed to concentrate on the sample, and the spectrum was collected by using 1800 lines per mm grating. The samples were placed in a liquid nitrogen-cooled Linkam cryostat for temperature-dependent measurement. The laser power was kept below 14 μW during the entire temperature-dependent measurements.

The first-principles density-functional theory (DFT) computations were completed by applying the Vienna *Ab initio* Simulation Package (VASP) [29,30] for monolayer and different stacking orders of bilayer MoSe<sub>2</sub>. For the purpose of describing the ion-electron interactions within the system, all-electron projector-augmented wave (PAW) potentials [31,32] were implemented. The electronic exchange and correlation component of the potential can be illustrated through the Perdew-Burke-Ernzerhof (PBE) [33] generalized gradient approximation. To avoid the spurious interactions between periodically repeated images and make the 2D sheet of monolayer and bilayer, a 15 Å vacuum along the *c* axis was used. In the basis sets for planar waves, the Kohn-Sham orbitals were expanded with an energy cutoff of 500 eV. The lattice parameters and atomic positions were optimized by taking into account the weak van der Waals (vdW) interactions between the layers, which are included in Grimme’s PBE-D2 [34], where the pairwise force field characterizes the weak vdW interactions. For relaxation, the Brillouin zone of the structures was sampled using a well-converged,  $\Gamma$ -centered Monkhorst-Pack [35] *k* grid of  $12 \times 12 \times 1$  for the monolayer and bilayers of MoSe<sub>2</sub>. The conjugate gradient approximation was used to optimize the monolayer and bilayers until the Hellmann-Feynman forces operating on each individual atom were smaller than 0.005 eV/Å. Applying the principles of density-functional perturbations theory (DFPT) [36], phonon dispersion was determined. PHONOPY [37], an extra package with a VASP interface that is based on the Parlinski-Li-Kawazoe approach, was utilized for phonon dispersion. The lattice thermal conductivity ( $\kappa_{\text{latt}}$ ) was obtained by direct solution of the linearized phonon Boltzmann transport equation [38,39] by considering the anharmonic terms up to third order with the help of PHONO3PY [39,40] code. The harmonic second- and third-order interatomic forces were computed with high accuracy of energy cutoff 500 eV and energy convergence criterion of  $10^{-8}$  eV. The super cells of  $3 \times 3 \times 1$

were considered to calculate the second- and third-order forces. The calculations of force constants were obtained by sampling the Brillouin zone (BZ) with a  $5 \times 5 \times 1$   $k$  grid. For  $\kappa_{\text{latt}}$ , a converged  $q$  grid of  $19 \times 19 \times 1$  was used for monolayer and bilayer  $\text{MoSe}_2$ . The Born-effective charges were taken into account for the long-range interactions, and the DFP principle was used to compute them.

### III. EXPERIMENTAL RESULTS AND DISCUSSION

The present literature raises a number of questions about the heat-transmission process in layered  $\text{MoSe}_2$  as well as other TMDCs [6–41]. The thermal conductivity of these systems exhibits significant changes during the transition from 1L to BL as well as multilayer systems. Although thermal conductivity is well studied in BL TMDCs, it is limited for the twisted configuration in the case of TMDCs. Recent study in twisted-bilayer black phosphorus (BP) shows a significant twist-induced change in thermal conductivity [42]. The anisotropy involved in the case of BP might be the cause of nonuniform thermal conductivity over the axis. Based on those observations, we could predict that thermal conductivity may vary over the twisted angle and stacking sequence in the case of isotropic materials like  $\text{MoS}_2$  and  $\text{MoSe}_2$ , owing to the change in BZ arrangement in the twisted configuration. To comprehend the proper mechanism of the heat-transfer method in the t-BL system ( $AB$ ,  $AB'$ , and intermediate twist angle), we have calculated the thermal conductivity of these systems by applying the optothermal Raman technique [8–27] by performing temperature- and power-dependent Raman measurements. This optothermal Raman approach has been proven to be a reliable and noncontact technique for determining the thermal conductivity of 2D materials [27]. This approach determines the exact location of a Raman-active mode by concentrating a monochromatic laser beam onto the flakes. Thermal softening facilitates the redshift of Raman modes when the laser power or sample temperature increases. The shift rate can be employed for determining thermal conductivity in the t-BL system with the help of thermal modeling. Twisted bilayer  $\text{MoSe}_2$  samples with different twist angles in the range of  $0 \leq \theta \leq 60^\circ$  were prepared by PMMA-based transfer technique. We were able to achieve t-BL of  $\text{MoSe}_2$  that had various interlayer stacking angles by transferring  $\text{MoSe}_2$  monolayers from one sapphire substrate as well as stacking them over another transferred  $\text{MoSe}_2$  monolayer (1L) on  $\text{SiO}_2$  [300-nm]/Si substrate. The equilateral-triangle shape of ML  $\text{MoSe}_2$  flakes helps us to measure the twist angles precisely (within an error limit of  $< 1^\circ$ ) using optical imaging. The OM images and the height profiles of some selected t-BL flakes confirmed by atomic force microscopy (AFM) topography are shown in Figs. 1(a)–1(f). Their representative height profiles are shown in Figs. S1, S1(a), and S1(b) (Supplemental Material [43]).

In a bilayer TMDC system, there are five high-symmetry stacking patterns that can occur at angles  $0^\circ$  and  $60^\circ$ , depending on the crystal structure of the individual layers and the relative position of the layers. Two high-symmetry stacking patterns,  $3R$  (often abbreviated as  $AB$ ) and  $AA$ , are present at  $0^\circ$  and three stacking patterns that have an excellent symmetry,  $2H$  (also known as  $AA'$ ),  $AB'$ , and  $A'B$  are present at  $60^\circ$ .

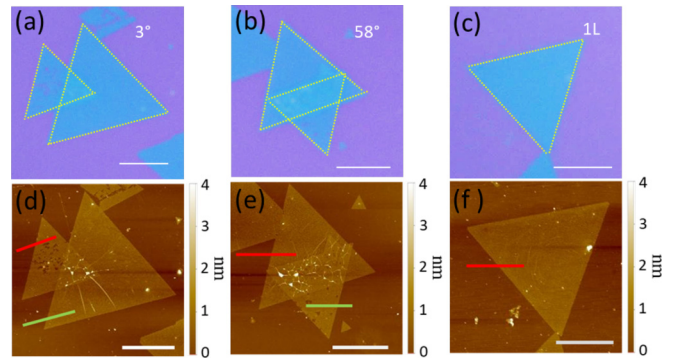


FIG. 1. (a)–(c) OM images of t-BL with stacking angles  $3^\circ$ ,  $58^\circ$ , and 1L  $\text{MoSe}_2$  flakes (scale bar, 5  $\mu\text{m}$ ), respectively. [(d)–(f)] Corresponding AFM images of t-BL with stacking angles  $3^\circ$ ,  $58^\circ$ , and 1L  $\text{MoSe}_2$  flakes (scale bar, 5  $\mu\text{m}$ ), respectively.

The stacking sequences such as  $AB$  and  $AB'$  are known to be the most stable configuration, which is generally found in the triangular 2D TMDCs grown by the CVD method [44]. These stackings correspond to the mutual twist angles of  $0^\circ$  and  $60^\circ$ , respectively. Figures 2(a) and 2(b) show the schematic of the stacking order in the top and side view. In artificial stacking, other intermediate twist angles are able to be found in addition to  $0^\circ$  and  $60^\circ$ . Hence, for better comparison, the measurements have been performed on an intermediate twist angle, i.e.,  $31^\circ$  along with the  $AB$  and  $AB'$  stacking. In our measurements, the stacking angles have slightly deviated from the exact angle orientation,  $0^\circ$  and  $60^\circ$ .  $AB$  has stacking as  $2^\circ$  and  $3^\circ$ , whereas for  $AB'$ , it is  $57^\circ$  and  $58^\circ$ , respectively. This considerable deviation has occurred as the samples are made by artificial stacking, as discussed in Sec. II. Figures 2(a) and 2(c) show the side and top view of high-symmetric stacking  $AB$ , which corresponds to the  $0^\circ$  stacking angle of bilayer  $\text{MoSe}_2$ , where Mo is placed over Se, and the other Mo and Se are placed over the hexagonal centers. Similarly, Figs. 2(b) and 2(d) show the side and top view of high-symmetric stacking  $AB'$ , which corresponds to the  $60^\circ$  stacking angle of bilayer  $\text{MoSe}_2$ , where Mo is positioned over Mo and all of Se is positioned over the hexagonal centers.

In order to characterize the t-BL  $\text{MoSe}_2$  and to confirm the stacking sequence, we have performed low-frequency (LF) Raman and photoluminescence (PL) measurements. Usually, LF Raman measurement is considered a unique deterministic technique to visualize stacking orientation and twist angle in 2D systems [45]. Figure 3(a), top and bottom panels, show the LF Raman spectra for  $58^\circ$  and  $3^\circ$  twist angles, respectively, as confirmed by the OM image [Figs. 1(a) and 1(b)]. In the case of  $58^\circ$ , the shear mode (S) and breathing mode (B) appear at  $18.9$  and  $28.9$   $\text{cm}^{-1}$ , respectively, whereas for  $3^\circ$  stacking, the S and B1 appear at  $17.9$  and  $34.6$   $\text{cm}^{-1}$ . The separation between S and B is  $11$  and  $10$   $\text{cm}^{-1}$ , which confirms the stacking sequence to be  $AB$  and  $AB'$ , as reported earlier [44]. Besides the mode separation, the relative intensity ratio  $S/B1 \sim 3/2$  for  $58^\circ$  and  $S/B2 \sim 1/4$  for  $3^\circ$  further confirms the stacking orientation as shown in the previous study for  $AB$  and  $AB'$  stacking. B1 and B2 are specific types of breathing modes that can be observed in low-frequency Raman spectra. B1 corresponds to the symmetric breathing mode, while B2

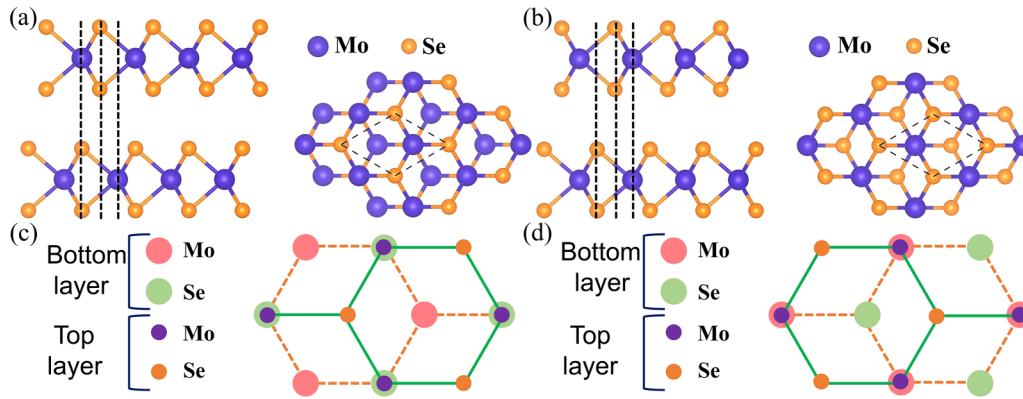


FIG. 2. (a), (b) Side and top view of stacking  $AB$  and  $AB'$  corresponds to  $0^\circ$  and  $60^\circ$  stacking angles of BL  $\text{MoSe}_2$ , respectively. Purple (orange) solid sphere corresponds to Mo (Se) atoms. For each twist angle, unit cell is shown, and its size varies strongly with angle. (c), (d) Top view of  $AB$  and  $AB'$  stacking corresponds to  $0^\circ$  and  $60^\circ$  for BL  $\text{MoSe}_2$ , respectively. Pink (green) solid circles correspond to Mo (Se) atoms at bottom layer, and purple (orange) circles correspond to Mo (Se) atoms at top layer.

corresponds to the antisymmetric breathing mode. In addition to the B2 mode, we have observed a significant contribution of the B1 mode for a  $3^\circ$  stacking angle. For  $AB'$  ( $60^\circ$ ) or close to  $60^\circ$  ( $> 55^\circ$ ), this contribution of B2 mode usually disappears [44]. In the present scenario,  $58^\circ$  stacking does not show the signature of B2 as shown in Fig. 3(a), top panel. For more confirmation, we have performed LF Raman for one intermediate angle of  $31^\circ$  as shown in Fig. S2 (Supplemental Material [43]), where both B1 and B2 modes are present with a separation of  $8 \text{ cm}^{-1}$ . The disappearance of the S mode for the intermediate twist angle confirms the stacking sequence of  $AB$  and  $AB'$  or close to  $0^\circ$  and  $60^\circ$  twist. Further, we have performed room-temperature PL measurements for F2 and F1 flakes, as shown in Fig. 3(b) upper and lower panels, respectively. PL measurement is also performed on the exposed 1L part of the twisted sample for better comparison. In the case of 1L  $\text{MoSe}_2$ , the main excitonic peak  $AX^0$  is dominating around  $\sim 789.5 \text{ nm}$  [ $\sim 1.57 \text{ eV}$ ], whereas for the

twisted-bilayer case,  $AX^0$  has been redshifted to 790.1 and 790 nm for  $58^\circ$  and  $3^\circ$ , respectively. Besides, the intensity has been significantly reduced for the case of BL due to the indirect band gap in nature. It can be noted that along with the A excitonic peak  $AX^0$ , trionic ( $AX^-$ ) contribution is also observed for the twisted case. The energy separation between  $AX^0$  and  $AX^-$  is found to be  $\sim 17$  and  $\sim 27 \text{ meV}$  for the case of  $58^\circ$  and  $3^\circ$ , respectively. This energy separation of bilayer  $\text{MoS}_2$  ( $\sim 20 \text{ meV}$ ) shows a similar trend at room temperature, as reported earlier [46]. A significant change in the relative contribution of the exciton ( $AX^0$ ) and trion ( $AX^-$ ) has been observed for  $3^\circ$  and  $58^\circ$  stacking., which may be due to the change of stacking orientation or lattice mismatch. For intermediate angle  $31^\circ$ ,  $AX^0$  appears at  $\sim 790.9 \text{ nm}$  as shown in Fig. S2 (Supplemental Material [43]), in which trion peak ( $AX^-$  at  $\sim 803.2 \text{ nm}$ ) peak dominates with an energy separation of  $\sim 23 \text{ meV}$ .

### A. Temperature-dependent Raman spectra

A 632.8-nm incident laser was employed to conduct the temperature-dependent Raman experiment for t-BL  $\text{MoSe}_2$  and 1L  $\text{MoSe}_2$ . Figure 4(a) shows the Raman spectra of nearly  $AB$ -stacked ( $3^\circ$ ) t-BL, with the change in temperature from 296 to 476 K. The laser power was maintained below  $15 \mu\text{W}$  to eliminate power-dependent thermal heating and keep it constant during the course of the experiment. For the optimal peak position, the Lorentz function was fitted to each Raman spectra. The redshift of the Raman  $A_{1g}$  peak is subsequently accompanied by a rise in temperature. Other twist angles of t-BL  $\text{MoSe}_2$  also show a similar trend for Raman spectra, but the amount of redshift varies with different twist angles [Figs. 4(a) and 4(b) and Figs. S3(a)–S3(c) (Supplemental Material [43])]. Figures 4(b) and 4(c) show the temperature-dependent Raman spectra for t-BL (nearly  $AB'$  stacked,  $58^\circ$ ) and 1L  $\text{MoSe}_2$ , respectively.

Similarly, such measurements have been carried out for other stacking angles  $2^\circ$ ,  $31^\circ$ ,  $57^\circ$  and another adjacent 1L  $\text{MoSe}_2$ , shown in Fig. S3 (Supplemental Material [43]). Figure 4(d) shows the variation of the  $A_{1g}$  peak location in relation to temperature for t-BL systems along with 1L

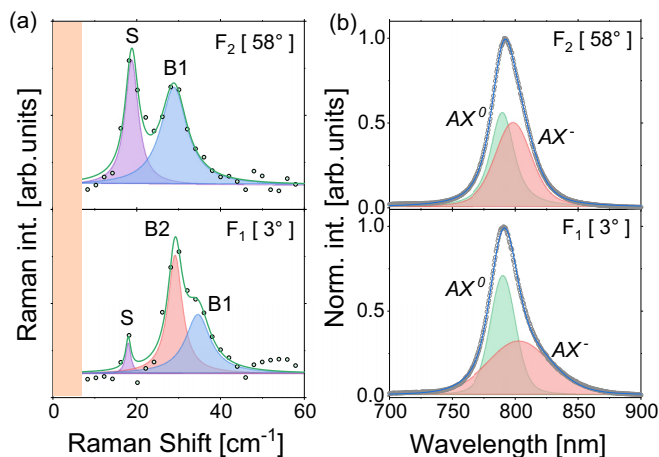


FIG. 3. (a) Stokes Raman spectra of low-frequency shear modes (SM) and breathing modes (LBM) for two different twist angles,  $3^\circ$  and  $58^\circ$ , respectively. (b) Photoluminescence of two different twist angles,  $3^\circ$  and  $58^\circ$ , respectively, which reflects changes in exciton and trion contributions.

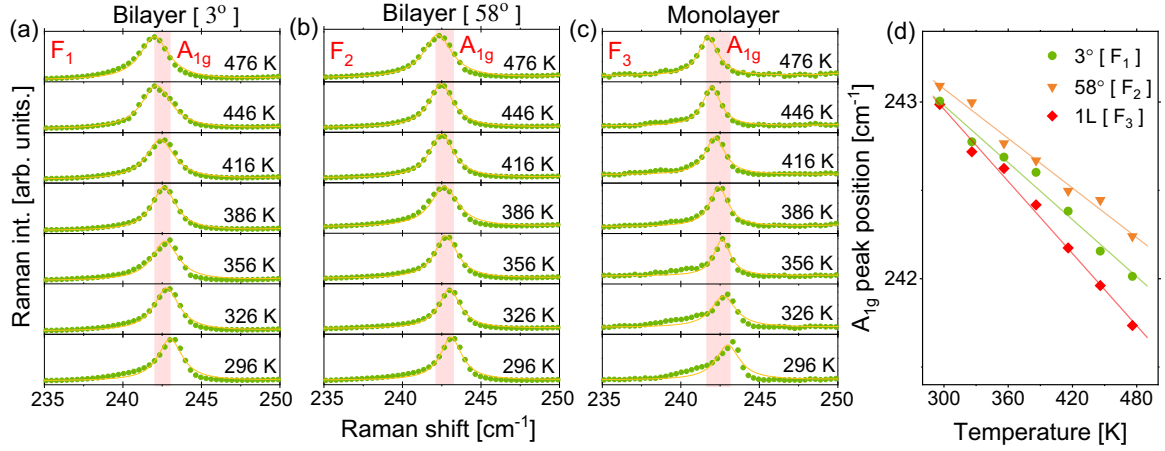


FIG. 4. (a)–(c) Raman spectra for t-BL system with stacking angles  $3^\circ$ ,  $58^\circ$ , and 1L MoSe<sub>2</sub> respectively, recorded in temperature range 296 to 476 K. (d) Temperature-dependent Raman shift of  $A_{1g}$  peak position for  $3^\circ$  (circle),  $58^\circ$  (triangle), and 1L MoSe<sub>2</sub> (square), respectively.

MoSe<sub>2</sub>. The variation in the peak position of  $A_{1g}$ , with respect to temperature for other stacking angles  $2^\circ$ ,  $31^\circ$ ,  $57^\circ$  and 1L MoSe<sub>2</sub>, are mentioned in Fig. S4 (Supplemental Material [43]). Being a function of lattice temperature, the modification that affects the Raman peak location  $\omega$  [in  $\text{cm}^{-1}$ ] exhibits a linear relationship [47], which is given by

$$\omega(T) = \omega_0 + \chi_T T, \quad (1)$$

where  $T$  represents temperature and the temperature coefficient of first order is  $\chi_T$ . At absolute-zero temperature, the vibration frequency corresponding to these phonon modes has been represented by  $\omega_0$ . The redshift that results from a temperature change (increase) can be attributed to thermally induced bond softening, as previously observed in graphene [8], which results in a change in Raman peak frequency. Hence, Eq. (1) becomes

$$\Delta\omega = \omega(T_2) - \omega(T_1) = \chi_T(T_2 - T_1) = \chi_T \Delta T, \quad (2)$$

where  $\Delta\omega$  is the change in frequency, and  $\Delta T$  is the change in temperature. The linear growth of phonon frequencies in t-BL and 1L MoSe<sub>2</sub> is driven by anharmonic lattice vibrations [48], which predominantly entail a contribution from the lattice's thermal expansion that resulted from the anharmonicity of the interatomic potential. The equilibrium sites of the atoms and, subsequently, the interatomic forces vary as the lattice expand or shrinks due to variations in temperature, which results in a change in the phonon energies [49].

### B. Power-dependent Raman spectra

The significance of the connection between laser power and the  $A_{1g}$  peak shift was investigated in the thermal conductivity study for both t-BL and 1L MoSe<sub>2</sub>. Figure 5(a) displays typical room-temperature (RT) Raman spectra that were acquired using a 632.8-nm incident laser with powers ranging from 5 to 63  $\mu\text{W}$  for t-BL MoSe<sub>2</sub> with stacking angle  $3^\circ$ . To determine the exact peak position, each Raman spectrum was fitted by employing the Lorentz function. Other stacking angles show a similar trend for Raman spectra, but the amount of redshift varies with different stacking angles.

The local heating of the t-BL and 1L MoSe<sub>2</sub> causes the  $A_{1g}$  Raman-active mode to soften as laser power rises.

Throughout the course of this study, the laser power was consistently maintained below 0.1 mW (below the saturation limit) and kept constant throughout the measurement within the linear dependency range. Figures 5(b) and 5(c) show the variation of the  $A_{1g}$  peak location in relation to power for t-BL systems along with 1L MoSe<sub>2</sub>. The variation in the peak position  $A_{1g}$ , with respect to power for other stacking angles  $2^\circ$ ,  $31^\circ$ ,  $57^\circ$  and another adjacent 1L MoSe<sub>2</sub>, are mentioned in Fig. S5 (Supplemental Material [43]), where the  $A_{1g}$  mode softens linearly with increasing power. The position of the peak as a function of power within the linear low-power range is depicted in Fig. 5(d) and Fig. S6 (Supplemental Material [43]), which is given by

$$\Delta\omega = \omega(P_2) - \omega(P_1) = \chi_P(P_2 - P_1) = \chi_P \Delta P. \quad (3)$$

Here, the power coefficient of first-order  $\chi_P$  is defined by the variation in the phonon frequency  $\omega$  with respect to incoming laser power  $P$  [ $\delta\omega/\delta P$ ]. The thermal conductivity of this t-BL system was measured using a noncontact technique by taking advantage of MoSe<sub>2</sub>'s phonon frequency's sensitive response to local laser heating. Despite not contributing considerably to direct heat transfer through the flake, Raman-active optical phonons demonstrate exceptional sensitivity to regional temperature fluctuation induced and regulated by external influences [50]. To determine the graphene's thermal conductivity, Balandin *et al.* [51] took into account the radial heat transfer and came up with the expression

$$\kappa = (1/2\pi h)(\nabla P/\nabla T), \quad (4)$$

where the change in the heating power  $\nabla P$  is what causes the local temperature rise  $\nabla T$  and the thickness of the material is represented by  $h$ . The thermal conductivity may be represented in the following manner by differentiating Eq. (1) with regard to power and replacing  $(\nabla P/\nabla T)$  into Eq. (4), which is provided by

$$\kappa = (1/2\pi h)\chi_T(\delta\omega/\delta P)^{-1}, \quad (5)$$

where  $\kappa$  is thermal conductivity, the temperature coefficient of first order is given by  $\chi_T$ , and the phonon frequency

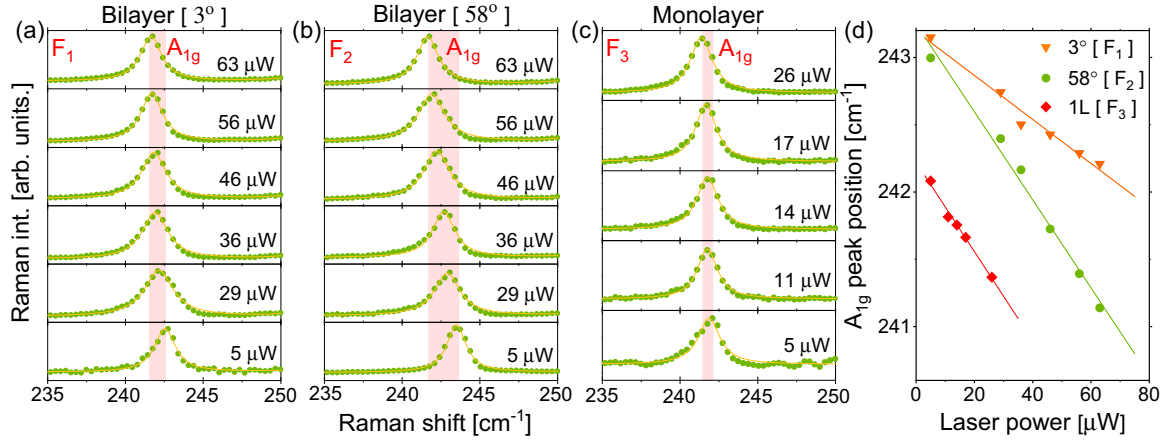


FIG. 5. (a)-(c) RT Raman spectra for t-BL system with stacking angles  $3^\circ$ ,  $58^\circ$ , and 1L MoSe<sub>2</sub>, respectively, recorded in laser power ranging from 5 to 63  $\mu\text{W}$ . (d) Power-dependent  $A_{1g}$  Raman peak shift for  $3^\circ$  (circle),  $58^\circ$  (triangle), and 1L MoSe<sub>2</sub> (square), respectively.

fluctuation with incoming laser power is provided by  $(\delta\omega/\delta P)$ . The sum of a material's "lattice thermal conductivity ( $\kappa_{\text{latt}}$ )" and "electronic thermal conductivity ( $\kappa_e$ )" is equal to its total thermal conductivity ( $\kappa$ ). The moment phonons, quantized lattice vibrations, are transported through a material, contributing to its thermal conductivity at the lattice level. However, the electrical component of thermal conductivity originates from the propagation of electrons and holes through the material. This contribution is typically dominant in metals and degenerate semiconductors, where the electrical conductivity is high. But, for nondegenerate semiconductors, lattice thermal conductivity mostly contributes to total thermal conductivity ( $\kappa \sim \kappa_{\text{latt}}$ ). For the purpose of determining the temperature and power coefficient of first order for each twist angle, the power- and temperature-dependent Raman experiments were carried out, from which the thermal conductivity of t-BL MoSe<sub>2</sub> was calculated, which is shown in Table I.

It is notable from Table I that the thermal conductivity of t-BL MoSe<sub>2</sub> (TMDC) varies with different twist angles. Angle-dependent thermal conductivities of  $2^\circ$  and  $3^\circ$  (near-*AB* stacking) have been calculated to be  $33 \pm 3$  and  $31 \pm 4 \text{ Wm}^{-1} \text{ K}^{-1}$ . Similarly, angle-dependent thermal conductivities of  $57^\circ$  and  $58^\circ$  (near-*AB'* stacking) have been calculated to be  $14 \pm 2$  and  $13 \pm 1 \text{ Wm}^{-1} \text{ K}^{-1}$ , respectively. For an intermediate angle ( $31^\circ$ ), the value is  $23 \pm 3 \text{ Wm}^{-1} \text{ K}^{-1}$ . So, the thermal conductivity value for t-BL MoSe<sub>2</sub> is reducing from 33 to  $13 \text{ Wm}^{-1} \text{ K}^{-1}$  with the change in twist angles.

The moiré superlattices within this twisted configuration contribute extra phonon scattering, which decreases the mean-free path of phonon and, consequently, the thermal conductivity. Apparently, when adjacent MoSe<sub>2</sub> layers are twisted, the number of atoms in the unit cell increases, which leads to an increment in the number of phonon vibration modes. This increment can reduce the phonon lifetime, as well as cause more phonons to scatter. In addition, the reduction in thermal conductivity found in t-BL MoSe<sub>2</sub> might be attributable to Brillouin-zone changes [52]. These modifications are caused by in-plane rotation, which results in the formation of many folded-phonon branches. The emergence of numerous folded-phonon branches in t-BL MoSe<sub>2</sub> enhances both phonon umklapp and normal scattering [53]. Umklapp phonon scattering occurs when phonons interact with each other and exchange momentum, resulting in the phonons being scattered in different directions. This scattering process can impede the heat flow and reduce the lattice thermal conductivity.

#### IV. THEORETICAL ANALYSIS

The thermal transport characteristics of BL MoSe<sub>2</sub> driven by stacking interactions were investigated by using first-principles DFT computations. The objective was to theoretically study the effect of stacking on thermal transport. As the phononic properties are key factors for determining a

TABLE I. Temperature coefficients of first-order, first-order power coefficients and room-temperature thermal conductivities of monolayer and t-BL MoSe<sub>2</sub>

Stacking angle [ $\theta$ ] (degree)	Temperature coefficient [ $\chi_T$ ] ( $\text{cm}^{-1} \text{ K}^{-1}$ )	Power coefficient [ $\chi_P$ ] ( $\text{cm}^{-1} \mu\text{W}^{-1}$ )	Thermal conductivity [ $\kappa$ ] ( $\text{Wm}^{-1} \text{ K}^{-1}$ )
Monolayer	$0.00685 \pm 0.00026$	$0.0339 \pm 0.0021$	$38 \pm 4$
Bilayer [ $2^\circ$ ]	$0.00543 \pm 0.00026$	$0.0153 \pm 0.0009$	$33 \pm 3$
Bilayer [ $3^\circ$ ]	$0.00538 \pm 0.00034$	$0.0163 \pm 0.0013$	$31 \pm 4$
Bilayer [ $31^\circ$ ]	$0.00504 \pm 0.00026$	$0.0204 \pm 0.0017$	$23 \pm 3$
Bilayer [ $57^\circ$ ]	$0.00472 \pm 0.00017$	$0.0311 \pm 0.0033$	$14 \pm 2$
Bilayer [ $58^\circ$ ]	$0.00468 \pm 0.00025$	$0.0327 \pm 0.0018$	$13 \pm 1$

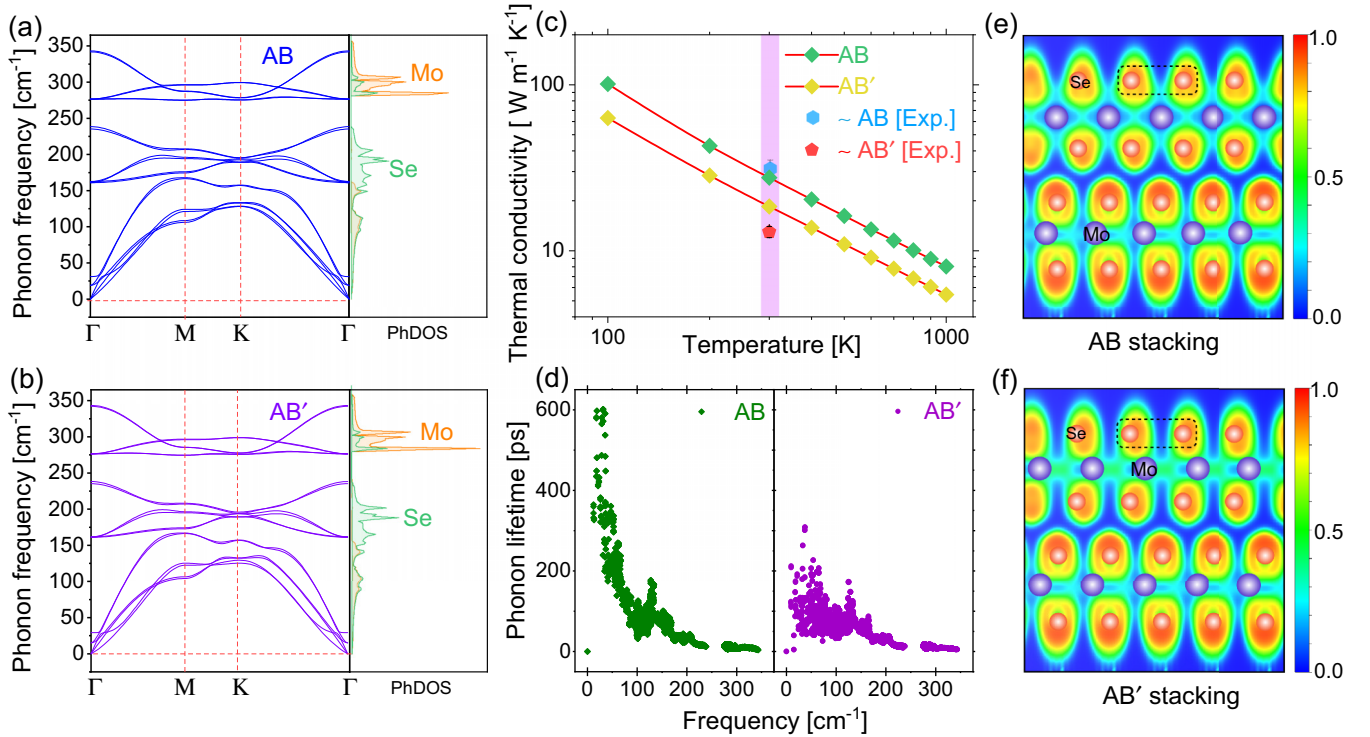


FIG. 6. Phonon dispersion (left panel) and PhDOS (right panel) for high-symmetric stacking (a) *AB* and (b) *AB'* of BL MoSe<sub>2</sub> stacked at 0° and 60°, respectively. (c) Theoretically calculated thermal conductivity of BL MoSe<sub>2</sub> as function of temperature for stacking sequence of *AB* and *AB'*, respectively. Experimentally obtained thermal conductivities of same stacking angles at RT are shown on highlighted (pink) region along theoretical values. (d) Phonon lifetime of BL MoSe<sub>2</sub> for *AB* and *AB'* stacking at RT. Corresponding projection of electron localization function along (100) plane of (e) *AB* and (f) *AB'* stacking order.

material's thermal transport, the phonon band structure for the *AB* and *AB'* stacked BL MoSe<sub>2</sub> has been computed and plotted in Figs. 6(a) and 6(b), respectively.

The phonon band structure study reveals the nonexistence of imaginary phonon modes in the phonon dispersions, demonstrating the stability of dynamics in both stacking configurations. There exists a finite phononic band gap in both the stacking orders over the frequency of  $\sim 234 \text{ cm}^{-1}$ , which plays an important role in determining the transport properties. Furthermore, the mass difference of Mo and Se in BL MoSe<sub>2</sub> indicates that the lower-phonon frequency modes are provided by the heavier cations Mo, and the higher-frequency modes by lighter anions Se, respectively. The phonon density of states (PhDOS) projected onto atoms was computed to evaluate the individual atoms' contributions towards phonon modes, as shown in the right panel of Figs. 6(a) and 6(b) for *AB* and *AB'* stacking orders, respectively. From the PhDOS of *AB* and *AB'* stacked BL MoSe<sub>2</sub>, it is observed that the low-frequency region in the range 0 to  $\sim 150 \text{ cm}^{-1}$  is contributed by both the Mo and Se atoms. Therefore, a hybridization of Mo and Se atoms is observed in this region, where all three acoustic modes, shear modes, and breathing modes are present. In the intermediate region (frequency range  $\sim 150$  to  $\sim 240 \text{ cm}^{-1}$ ), low-lying optical modes are present, including  $A_{1g}$  Raman mode. The theoretically predicted position of the  $A_{1g}$  Raman mode is  $242 \text{ cm}^{-1}$ , which is quite similar to the observed  $A_{1g}$  mode peak position. In this intermediate region, the phonon vibration is solely contributed by the Se atom. In the

high-frequency region, phonon modes ( $\sim 275$  to  $\sim 340 \text{ cm}^{-1}$ ) are caused by the vibrations of both the Mo and Se atoms. Similar to the low-frequency region, the hybridization of Mo and Se atoms in the lattice vibration is observed in this region. Finally, the lattice thermal conductivity ( $\kappa_{\text{latt}}$ ) is calculated for *AB* and *AB'* stacked BL MoSe<sub>2</sub> by computing the Boltzmann transport equation (BTE) for phonons. The values of  $\kappa_{\text{latt}}$  for *AB* and *AB'* stacking are  $27.56$  and  $18.50 \text{ W m}^{-1} \text{ K}^{-1}$ , respectively, at room temperature (300 K), which accord well with our experiments' results as plotted in Fig. 6(c). Therefore, a large reduction of  $\kappa_{\text{latt}}$  is observed by changing the stacking order from *AB* to *AB'* in BL MoSe<sub>2</sub>, as observed from our experimental as well as theoretical calculations. The temperature effect on the thermal transport of *AB* and *AB'* stacked BL MoSe<sub>2</sub>, the  $\kappa_{\text{latt}}$ , is calculated at various temperatures in the 100 to 1000 K range. For *AB* stacking, the value of  $\kappa_{\text{latt}}$  decreases from  $101.02$  to  $8.04 \text{ W m}^{-1} \text{ K}^{-1}$  when temperature varies from 100 to 1000 K, nearing the theoretical minimum value, with a predicted  $1/T$  dependency [54]. For *AB'* stacking, this value decreases from  $63.04$  to  $5.45 \text{ W m}^{-1} \text{ K}^{-1}$  when the temperature changes from 100 to 1000 K. The variation of  $\kappa_{\text{latt}}$  with temperature is demonstrated in Figs. S7(a) and S7(b) (Supplemental Material [43]) for *AB* and *AB'* stacked BL MoSe<sub>2</sub>, respectively. With the increase in temperature, the value of  $\kappa_{\text{latt}}$  decreases very fast in the low-temperature range and almost saturates beyond a certain temperature ( $\sim 500 \text{ K}$ ). This is due to the rapid increase of thermal scattering with temperature, which saturates after a certain higher

value of temperature. The log-log plot of  $\kappa_{\text{latt}}$  with respect to temperature is shown in Fig. 6(c), which reveals the similarity of thermal transport in both the stacking orders and indicates that both the stacking order possesses identical variation of  $\kappa_{\text{latt}}$  with temperature by a constant shift of  $\Delta\kappa_{\text{latt}}$  in the log scale. Although the different stacking order makes the difference in  $\kappa_{\text{latt}}$  value, it has a similar effect of temperature on  $\kappa_{\text{latt}}$  as well as the thermal scattering. In order to elucidate the fundamental root cause, the stacking-dependent lattice thermal conductivity ( $\kappa_{\text{latt}}$ ) of bilayer MoSe<sub>2</sub> has been calculated. We considered the Peierls-Boltzmann transport equation solution obtained under relaxation-time approximation [55,56] in the kinetic theory as the lattice thermal conductivity equation written as [53–57]

$$\kappa_{\text{latt}} = \frac{1}{NV_C} \sum C_\lambda v_\lambda \otimes v_\lambda \tau_\lambda^{\text{SMRT}}, \quad (6)$$

where  $\tau_\lambda^{\text{SMRT}}$  is single-mode relaxation time (SMRT) and  $C_\lambda$  is mode heat capacity.  $C_\lambda$  and  $v_\lambda$  are computed from the harmonic phonon calculation. As the stacking order in the multilayer and heterostructure determines the intralayer and interlayer interactions between the constituent atoms [58,59], it has a significant effect on the phonon scattering. Therefore, both the lifetime ( $\tau$ ) and group velocity ( $v_g$ ) of phonon, two fundamental physical parameters, might be affected by the change in stacking order. To further understand the influence of stacking order on thermal conductivity, the electron localization function (ELF) and phonon lifetime were determined.

### A. Phonon lifetime

The phonon lifetime for *AB* and *AB'* stacked MoSe<sub>2</sub> at 300 K is shown in Fig. 6(d), left and right panels, respectively. The phonon lifetime represents the total time for heat carrying by phonons before the scattering. Therefore,  $\kappa_{\text{latt}}$  has a direct proportionality relation with phonon lifetime ( $\tau$ ) as indicated in Eq. (6). Therefore, the higher  $\kappa_{\text{latt}}$  results from the longer phonon lifetime [60,61]. Phonon lifetime for *AB* stacking is found in the range of 0 to  $\sim 600$  ps, whereas for *AB'* stacking it is in the range of 0 to  $\sim 300$  ps. Therefore, the maximum limit of the phonon lifetime is reduced significantly when stacking order changes from *AB* to *AB'* in BL MoSe<sub>2</sub>. Hence, the average heat carrying by phonons in the *AB* stacking is more than *AB'* stacking, leading to higher  $\kappa_{\text{latt}}$ . This is also applicable to other temperatures of the system. As a result of this, at any temperature in the range (100 to 1000 K) the value of  $\kappa_{\text{latt}}$  is more in *AB* stacking than *AB'* stacking.

### B. Electron localization function

The ELF [62,63] was studied in order to better comprehend the bonding in the bilayer system. ELF estimates the likelihood of finding an electron close to the reference electron. The limitations for entirely localized and extremely delocalized electrons are represented by the ELF's values of 1 and 0, respectively. The ELF projected along [100] for *AB* and *AB'* stacking has been shown in Figs. 6(e) and 6(f), respectively. In both stackings, the bottom layer is fixed, while the top layer is displaced and rotated with respect to the bottom layer

depending upon the stacking order. Therefore, we can find the identical ELF of the lower layer in both the stacking orders, whereas there is finite difference between the ELF of the top layer of *AB* and *AB'* stacking, as shown in Figs. 6(e) and 6(f). This difference creates differences in the thermal transport properties of the *AB* and *AB'* stacking. For the  $\kappa_{\text{latt}}$ , the low-frequency and medium-frequency range of lattice vibration plays a major role. Our experiment results also suggest the contribution of  $A_{1g}$  Raman mode on the  $\kappa_{\text{latt}}$ , which lies in the medium-frequency range. In this frequency range, mainly the vibration is due to the Se atoms, as shown in the right panel of Figs. 6(a) and 6(b) for *AB* and *AB'* stacking, respectively. Therefore, the ELF between consecutive Se atoms is a major concern for the thermal transport of the lattice vibration. From Fig. 6(e), it is observed that in between the Se atoms, there exists a finite electron localization in *AB* stacking order (dotted black box region). On the contrary, the electron localization in *AB'* stacking order is significantly weak, as shown in Fig. 6(f). The high electron localization facilitates the  $\kappa_{\text{latt}}$  in the system [61]. The relatively stronger electron localization increases the phonon group velocity and assists to increase  $\kappa_{\text{latt}}$  with the phonon lifetime for *AB* stacking rather than *AB'* stacking. Along with *AB* and *AB'* stacking, Fig. S8 (Supplemental Material [43]) also depicts the electron localization for the intermediate stacking angle. From the electron localization for the intermediate stacking angle, it can be seen that the strength of the electron localization between Se atoms is stronger than *AB'* but weaker than *AB* stacking. This is the reason for higher and lower values of thermal conductivity in intermediate stacking angle than *AB'* and *AB* stacking, respectively. For better understanding, a comparative study of thermal conductivity for 1L and BL MoSe<sub>2</sub> (both theoretical and experimental) is given in Fig. S9 (Supplemental Material [43]).

## V. CONCLUSION

We have synthesized t-BL MoSe<sub>2</sub> with different twist angles using APCVD followed by the wet-transfer method. The optothermal Raman approach was implemented to calculate the thermal conductivity of 1L and t-BL systems at ambient temperature. The thermal conductivity varying as a function of different twist angles has been addressed. The observed thermal conductivity values are found to be  $13 \pm 1$ ,  $23 \pm 3$  and,  $30 \pm 4 \text{ Wm}^{-1} \text{ K}^{-1}$  for twist angle  $[\theta] = 58^\circ$ ,  $31^\circ$ , and  $3^\circ$ , respectively. The thermal conductivity of 1L ( $38 \pm 4 \text{ Wm}^{-1} \text{ K}^{-1}$ ) is found to be larger than the bilayer due to the decrease in phonon scattering at the interface between layers. Theoretically, the estimated thermal conductivity of bilayer MoSe<sub>2</sub> for *AB* and *AB'* stacking orders using the phonon BTE strongly supports the experimental results. Furthermore, the theoretical DFPT calculations and ELF analysis explore the fundamental origin of twist angle-dependent thermal conductivity in t-BL MoSe<sub>2</sub>. The change in twist angle in t-BL MoSe<sub>2</sub> exhibits the twist angle-driven thermal conductivity, which may be attributed to changes in both the group velocity and the lifetime of phonons. The findings show more precise thermal transport measurements in the t-BL (homobilayer 2D) system, a significant paradigm for device modeling and other applications.

## ACKNOWLEDGMENTS

P.K.N. acknowledges the financial support from the Ministry of Human Resource Development (MHRD), Government of India (GOI) via STARS Grant No. STARS/APR2019/148 and Department of Science and Technology, Government of India (DST-GoI), with Sanction Order No. SB/S2/RJN-043/2017 under Ramanujan Fellowship. P.K.N. also acknowledges the support from the Institute of Eminence scheme at IIT-Madras, through the 2D Materials

Research and Innovation Group and N.M., A.S., and A.K.S. thank the Materials Research Centre (MRC) and the Solid State and Structural Chemistry Unit (SSCU), Indian Institute of Science for the computational facilities. A.S. acknowledges support by DST-INSPIRE Fellowship No. IF190068. N.M., A.S., and A.K.S. also acknowledge the support from the Institute of Eminence (IoE) scheme of The Ministry of Human Resource Development (MHRD), Government of India.

- 
- [1] Y. Kuang, L. Lindsay, S. Shi, X. Wang, and B. Huang, Thermal conductivity of graphene mediated by strain and size, *Int. J. Heat Mass Transfer* **101**, 772 (2016).
- [2] F. Yousefi, F. Khoeini, and A. Rajabpour, Thermal conductivity and thermal rectification of nanoporous graphene: A molecular dynamics simulation, *Int. J. Heat Mass Transfer* **146**, 118884 (2020).
- [3] F. Liu, Y. Wang, X. Liu, J. Wang, and H. Guo, Ballistic transport in monolayer black phosphorus transistors, *IEEE Trans. Electron Devices* **61**, 3871 (2014).
- [4] X. Wang *et al.*, Recent advances in the functional 2d photonic and optoelectronic devices, *Adv. Opt. Mater.* **7**, 1801274 (2019).
- [5] R. E. Munteanu, P. S. Moreno, M. Bramini, and S. Gáspár, 2D materials in electrochemical sensors for in vitro or in vivo use, *Anal. Bioanal. Chem.* **413**, 701 (2021).
- [6] Y. Dong, Z. S. Wu, W. Ren, H. M. Cheng, and X. Bao, Graphene: A promising 2d material for electrochemical energy storage, *Sci. Bull.* **62**, 724 (2017).
- [7] A. M. Dubrovkin, B. Qiang, H. N. S. Krishnamoorthy, N. I. Zheludev, and Q. J. Wang, Ultra-confined surface phonon polaritons in molecular layers of van der Waals dielectrics, *Nat. Commun.* **9**, 1762 (2018).
- [8] I. Calizo, A. A. Balandin, W. Bao, F. Miao, and C. N. Lau, Temperature dependence of the raman spectra of graphene and graphene multilayers, *Nano Lett.* **7**, 2645 (2007).
- [9] Q. H. Wang, K. Kalantar-Zadeh, A. Kis, J. N. Coleman, and M. S. Strano, Electronics and optoelectronics of two-dimensional transition metal dichalcogenides, *Nat. Nanotechnol.* **7**, 699 (2012).
- [10] A. A. Balandin, Thermal properties of graphene and nanostructured carbon materials, *Nat. Mater.* **10**, 569 (2011).
- [11] S. Das, H. Y. Chen, A. V. Penumatcha, and J. Appenzeller, High performance multilayer MoS<sub>2</sub> transistors with scandium contacts, *Nano Lett.* **13**, 100 (2013).
- [12] B. Radisavljevic and A. Kis, Mobility engineering and a metal-insulator transition in monolayer MoS<sub>2</sub>, *Nat. Mater.* **12**, 815 (2013).
- [13] B. W. H. Baugher, H. O. H. Churchill, Y. Yang, and P. Jarillo-Herrero, Intrinsic electronic transport properties of high-quality monolayer and bilayer MoS<sub>2</sub>, *Nano Lett.* **13**, 4212 (2013).
- [14] H. Wang, L. Yu, Y. H. Lee, Y. Shi, A. Hsu, M. L. Chin, L. J. Li, M. Dubey, J. Kong, and T. Palacios, Integrated circuits based on bilayer MoS<sub>2</sub> transistors, *Nano Lett.* **12**, 4674 (2012).
- [15] J. Yoon *et al.*, Highly flexible and transparent multilayer MoS<sub>2</sub> transistors with graphene electrodes, *Small* **9**, 3185 (2013).
- [16] K. F. Mak, C. Lee, J. Hone, J. Shan, and T. F. Heinz, Atomically Thin MoS<sub>2</sub>: A New Direct-Gap Semiconductor, *Phys. Rev. Lett.* **105**, 136805 (2010).
- [17] R. S. Sundaram, M. Engel, A. Lombardo, R. Krupke, A. C. Ferrari, P. Avouris, and M. Steiner, Electroluminescence in single layer MoS<sub>2</sub>, *Nano Lett.* **13**, 1416 (2013).
- [18] D. Jariwala, V. K. Sangwan, L. J. Lauhon, T. J. Marks, and M. C. Hersam, Emerging device applications for semiconducting two-dimensional transition metal dichalcogenides, *ACS Nano* **8**, 1102 (2014).
- [19] G. H. Lee *et al.*, Flexible and transparent MoS<sub>2</sub> field-effect transistors on hexagonal boron nitride-graphene heterostructures, *ACS Nano* **7**, 7931 (2013).
- [20] H. Zeng, J. Dai, W. Yao, D. Xiao, and X. Cui, Valley polarization in MoS<sub>2</sub> monolayers by optical pumping, *Nat. Nanotechnol.* **7**, 490 (2012).
- [21] M. Sup Choi, G. H. Lee, Y. J. Yu, D. Y. Lee, S. Hwan Lee, P. Kim, J. Hone, and W. J. Yoo, Controlled charge trapping by molybdenum disulphide and graphene in ultrathin heterostructured memory devices, *Nat. Commun.* **4**, 1624 (2013).
- [22] C. Lee, H. Yan, L. E. Brus, T. F. Heinz, J. Hone, and S. Ryu, Anomalous lattice vibrations of single- and few-layer MoS<sub>2</sub>, *ACS Nano* **4**, 2695 (2010).
- [23] S. Kim *et al.*, High-mobility and low-power thin-film transistors based on multilayer MoS<sub>2</sub> crystals, *Nat. Commun.* **3**, 1011 (2012).
- [24] X. Zhang, D. Sun, Y. Li, G. H. Lee, X. Cui, D. Chenet, Y. You, T. F. Heinz, and J. C. Hone, Measurement of lateral and interfacial thermal conductivity of single- and bilayer MoS<sub>2</sub> and MoSe<sub>2</sub> using refined optothermal raman technique, *ACS Appl. Mater. Interfaces* **7**, 25923 (2015).
- [25] B. Peng, H. Zhang, H. Shao, Y. Xu, X. Zhang, and H. Zhu, Thermal conductivity of monolayer MoS<sub>2</sub>, MoSe<sub>2</sub>, and WS<sub>2</sub>: Interplay of mass effect, interatomic bonding and anharmonicity, *RSC Adv.* **6**, 5767 (2016).
- [26] X. Gu and R. Yang, Phonon transport in single-layer transition metal dichalcogenides: A first-principles study, *Appl. Phys. Lett.* **105**, 131903 (2014).
- [27] W. Cai, A. L. Moore, Y. Zhu, X. Li, S. Chen, L. Shi, and R. S. Ruoff, Thermal transport in suspended and supported monolayer graphene grown by chemical vapor deposition, *Nano Lett.* **10**, 1645 (2010).
- [28] P. K. Nayak *et al.*, Probing evolution of twist-angle-dependent interlayer excitons in MoSe<sub>2</sub>/WSe<sub>2</sub> van der Waals heterostructures, *ACS Nano* **11**, 4041 (2017).

- [29] G. Kresse and J. Furthmüller, Efficient iterative schemes for *ab initio* total-energy calculations using a plane-wave basis set, *Phys. Rev. B* **54**, 11169 (1996).
- [30] G. Kresse and J. Furthmüller, Efficiency of *ab-initio* total energy calculations for metals and semiconductors using a plane-wave basis set, *Comput. Mater. Sci.* **6**, 15 (1996).
- [31] P. E. Blochl, Projector augmented-wave method, *Phys. Rev. B* **50**, 17953 (1994).
- [32] G. Kresse and D. Joubert, From ultrasoft pseudopotentials to the projector augmented-wave method, *Phys. Rev. B* **59**, 1758 (1999).
- [33] J. P. Perdew, K. Burke, and M. Ernzerhof, Generalized Gradient Approximation Made Simple, *Phys. Rev. Lett.* **77**, 3865 (1996).
- [34] S. Grimme, Semiempirical GGA-type density functional constructed with a long-range dispersion correction, *J. Comput. Chem.* **27**, 1787 (2006).
- [35] H. J. Monkhorst and J. D. Pack, Special points for brillouin-zone integrations, *Phys. Rev. B* **13**, 5188 (1976).
- [36] X. Gonze and J. P. Vigneron, Density-functional approach to nonlinear-response coefficients of solids, *Phys. Rev. B* **39**, 13120 (1989).
- [37] A. Togo and I. Tanaka, First principles phonon calculations in materials science, *Scr. Mater.* **108**, 1 (2015).
- [38] L. Chaput, Direct solution to the linearized phonon boltzmann equation, *Phys. Rev. Lett.* **110**, 265506 (2013).
- [39] A. Togo, L. Chaput, and I. Tanaka, Distributions of phonon lifetimes in brillouin zones, *Phys. Rev. B* **91**, 094306 (2015).
- [40] A. Togo, First-principles phonon calculations with phonopy and Phono3py, *J. Phys. Soc. Jpn.* **92**, 012001 (2023).
- [41] E. Easy, Y. Gao, Y. Wang, D. Yan, S. M. Goushegir, E. H. Yang, B. Xu, and X. Zhang, Experimental and computational investigation of layer-dependent thermal conductivities and interfacial thermal conductance of one- to three-layer WSe<sub>2</sub>, *ACS Appl. Mater. Interfaces* **13**, 13063 (2021).
- [42] S. Duan, Y. Cui, W. Yi, X. Chen, B. Yang, and X. Liu, Enhanced thermoelectric performance in black phosphorene via tunable interlayer twist, *Small* **18**, 2204197 (2022).
- [43] See Supplemental Material at <http://link.aps.org/supplemental/10.1103/PhysRevB.108.115439> for OM images, AFM images and height profile, low-frequency Raman and PL for 31° t-BL MoSe<sub>2</sub>, temperature- and power-dependent Raman shift, and temperature and power coefficient for 3°, 31°, and 57° t-BL MoSe<sub>2</sub>, theoretical thermal conductivity as a function of temperature and ELF for AB and AB' stacking, and comparison of thermal conductivity of 1L and BL MoSe<sub>2</sub> with existing literature. It also contains Refs. [24–26,64,65].
- [44] A. A. Puretzy, L. Liang, X. Li, K. Xiao, B. G. Sumpter, V. Meunier, and D. B. Geohegan, Twisted MoSe<sub>2</sub> bilayers with variable local stacking and interlayer coupling revealed by low-frequency raman spectroscopy, *ACS Nano* **10**, 2736 (2016).
- [45] A. A. Puretzy *et al.*, Low-frequency raman fingerprints of two-dimensional metal dichalcogenide layer stacking configurations, *ACS Nano* **9**, 6333 (2015).
- [46] J. Pei *et al.*, Exciton and trion dynamics in bilayer MoS<sub>2</sub>, *Small* **11**, 6384 (2015).
- [47] M. P. Singh, M. Mandal, K. Sethupathi, M. S. R. Rao, and P. K. Nayak, Study of thermometry in two-dimensional Sb<sub>2</sub>Te<sub>3</sub> from temperature-dependent raman spectroscopy, *Nanoscale Res. Lett.* **16**, 22 (2021).
- [48] R. A. Cowley, The lattice dynamics of an anharmonic crystal, *Adv. Phys.* **12**, 421 (1963).
- [49] T. Beechem, S. Graham, S. P. Kearney, L. M. Phinney, and J. R. Serrano, Invited article: simultaneous mapping of temperature and stress in microdevices using micro-raman spectroscopy, *Rev. Sci. Instrum.* **78**, 061301 (2007).
- [50] R. Yan, J. R. Simpson, S. Bertolazzi, J. Brivio, M. Watson, X. Wu, A. Kis, T. Luo, A. R. Hight Walker, and H. G. Xing, Thermal conductivity of monolayer molybdenum disulfide obtained from temperature-dependent raman spectroscopy, *ACS Nano* **8**, 986 (2014).
- [51] A. A. Balandin, S. Ghosh, W. Bao, I. Calizo, D. Teweldebrhan, F. Miao, and C. N. Lau, Superior thermal conductivity of single-layer graphene, *Nano Lett.* **8**, 902 (2008).
- [52] A. I. Cocemasov, D. L. Nika, and A. A. Balandin, Phonons in twisted bilayer graphene, *Phys. Rev. B* **88**, 035428 (2013).
- [53] J. M. Ziman, *Electrons and Phonons* (Oxford University Press, New York, 2001).
- [54] D. G. Cahill, S. K. Watson, and R. O. Pohl, Lower limit to the thermal conductivity of disordered crystals, *Phys. Rev. B* **46**, 6131 (1992).
- [55] R. Peierls, Zur kinetischen theorie der wärmeleitung in kristallen, *Ann. Phys.* **395**, 1055 (1929).
- [56] P. B. Allen and V. Perebeinos, Temperature in a peierls-boltzmann treatment of nonlocal phonon heat transport, *Phys. Rev. B* **98**, 085427 (2018).
- [57] G. P. Srivastava, *The Physics of Phonons*, 2nd ed. (CRC Press, Boca Raton, 2022).
- [58] Y. Zhou *et al.*, Stacking-order-driven optical properties and carrier dynamics in ReS<sub>2</sub>, *Adv. Mater.* **32**, 1908311 (2020).
- [59] N. Maity, P. Srivastava, H. Mishra, R. Shinde, and A. K. Singh, Anisotropic interlayer exciton in GeSe/SnS van der Waals heterostructure, *J. Phys. Chem. Lett.* **12**, 1765 (2021).
- [60] M. Mukherjee and A. K. Singh, Strong chemical bond hierarchy leading to exceptionally high thermoelectric figure of merit in oxychalcogenide AgBiTeO, *ACS Appl. Mater. Interfaces* **12**, 8280 (2020).
- [61] A. Srivastava, M. Mukherjee, and A. K. Singh, Decoupled atomic contribution boosted high thermoelectric performance in mixed cation spinel oxides ACo<sub>2</sub>O<sub>4</sub>, *Appl. Phys. Lett.* **120**, 243901 (2022).
- [62] M. Mukherjee, G. Yumnam, and A. K. Singh, High thermoelectric figure of merit via tunable valley convergence coupled low thermal conductivity in A<sup>II</sup>B<sup>IV</sup>C<sub>2</sub><sup>V</sup> chalcopyrites, *J. Phys. Chem. C* **122**, 29150 (2018).
- [63] M. Mukherjee, A. Srivastava, and A. K. Singh, Recent advances in designing thermoelectric materials, *J. Mater. Chem. C* **10**, 12524 (2022).
- [64] S. Kumar and U. Schwingenschlögl, Thermoelectric response of bulk and monolayer MoSe<sub>2</sub> and WSe<sub>2</sub>, *Chem. Mater.* **27**, 1278 (2015).
- [65] A. Kandemir, H. Yapicioglu, A. Kinaci, T. Çağın, and C. Sevik, Thermal transport properties of MoS<sub>2</sub> and MoSe<sub>2</sub> monolayers, *Nanotechnology* **27**, 055703 (2016).